JOURNAL OF AIRCRAFT
Vol. 44, No. 4, July–August 2007

Supersonic Nonlinear Panel Flutter Suppression Using Shape Memory Alloys

Xinyun Guo*
Daniel Webster College, Nashua, New Hampshire 03063
Yiu-Yin Lee†
City University of Hong Kong, Kowloon, Hong Kong, People's Republic of China
and
Chuh Mei‡
Old Dominion University, Norfolk, Virginia 23529

DOI: 10.2514/1.16080

An efficient finite element procedure is developed to predict large-amplitude nonlinear flutter response of shape memory alloy hybrid composite plates at an arbitrary supersonic yawed angle and an elevated temperature. The temperature-dependent material properties of shape memory alloy and traditional composites, as well as the von Kármán large deflections, are considered in the formulation. Finite element system equations of motion are transferred to aeroelastic modal coordinates to reduce the large number of structural-node degrees of freedom. Time-domain numerical integration is employed to analyze flutter behaviors of the shape memory alloy hybrid composite panel under thermal loads. The flutter stability regions under the combined aerodynamic and thermal loads are studied. All of the possible behaviors, including the two types of static behavior and four types of dynamic motion of flutter, can be predicted for shape memory alloy hybrid composite plates. The static behaviors are 1) flat and stable and 2) aerothermally buckled but dynamically stable. The four types of dynamic motion are nearly simple harmonic limit-cycle oscillation, periodic limit-cycle oscillation, quasi-periodic oscillation, and chaotic oscillation. The flutter response of shape memory alloy hybrid composite plates are compared with those of traditional composite plates without a shape memory alloy. Results show that the desired flat and stable region can be greatly enlarged by using a shape memory alloy.

Nomenclature

$[A]$, $[B]$, $[D]$	=	in-plane, coupling, and bending laminate stiffness matrices
$[A_a]$	=	aerodynamic influence matrices
C_a	=	aerodynamic damping coefficient
$[G]$	=	aerodynamic damping matrix
$[\bar{G}]$	=	modal aerodynamic damping matrix
g_a	=	nondimensional aerodynamic damping
h	=	plate thickness
$[K]$	=	stiffness matrix
$[\bar{K}]$	=	modal linear stiffness matrix
$[K_{\text{lin}}]$	=	linear stiffness matrix
$[\bar{K}_q]$, $[\bar{K}_{qq}]$	=	modal nonlinear stiffness matrices
$[K_1]$, $[K_2]$	=	first-order and second-order nonlinear bending stiffness matrices
$[K1]$, $[K2]$	=	first-order and second-order nonlinear stiffness matrices
$[M]$	=	mass matrix
$[\bar{M}_b]$	=	modal bending mass matrix
M_∞	=	Mach number
$\{N\}$, $\{M\}$	=	force and moment vectors
$\{\bar{P}\}$	=	modal force vector
P_a	=	aerodynamic pressure
$[\bar{Q}]$	=	transformed lamina reduced-stiffness matrix
q	=	dynamic pressure/modal coordinate
T	=	temperature
u, v	=	incremental in-plane displacements
v_s, v_m	=	volume fractions of SMA and traditional composite matrix
V	=	airflow velocity
$\{W\}$	=	incremental nodal displacement vector
w	=	incremental transverse displacement
x, y, z	=	Cartesian coordinates
$\{\alpha\}$	=	thermal expansion coefficient vector
ΔT	=	temperature change
$\{\varepsilon\}$	=	strain vector
$\{\kappa\}$	=	bending curvature vector
Λ	=	flow yaw angle
λ	=	nondimensional dynamic pressure
μ	=	air-panel mass ratio
ρ	=	mass density
$\{\sigma\}$	=	stress vector
$[\Phi]$	=	eigenvector matrix
$\{\phi_r\}$	=	eigenvector

Subscripts

b	=	bending
cr	=	critical
m	=	membrane/composite matrix
NB	=	stiffness matrices due to $\{N_b\}$
Nm	=	stiffness matrices due to $\{N_m\}$
$N\Delta T$	=	stiffness matrices due to $\{N_{\Delta T}\}$
r	=	recovery stress of shape memory alloy
s	=	static/quantity related to shape memory alloy
ΔT	=	thermal

Presented as Paper 2372 at the 46th AIAA/ASME/ASCE/AHS/ASC Structures, Structural Dynamics and Materials Conference, Austin, TX, 18–21 April 2005; received 14 July 2005; revision received 2 January 2007; accepted for publication 24 February 2007.

*Assistant Professor, Division of Engineering, Mathematics and Science; guo_david@dwc.edu. Member AIAA.
†Associate Professor, Department of Building and Construction; bcraylee@cityu.edu.hk.
‡Professor, Department of Aerospace Engineering; cmei@odu.edu. Associate Fellow AIAA.

Introduction

THE surface panels of high-speed aircraft and spacecraft would exhibit large-amplitude panel flutter under high dynamic pressure and possibly display buckling at elevated temperatures. For example, the skin-panel temperature could reach up to 350°F (177°C) for the Quiet Supersonic Platform (QSP) cruising at Mach 2.2–2.4. Dowell [1] had an excellent review on both analytical and experimental research aspects of panel flutter in 1975. In 1999, Mei et al. [2] gave a review of nonlinear panel flutter at supersonic and hypersonic speeds.

Various classical analysis methods have been employed for panel flutter. The most often used partial differential equation (PDE)/Galerkin method adopted an approach that reduces the governing partial differential equations to a set of coupled ordinary differential equations by employing a set of linear normal modes (NMs) that satisfy the boundary conditions. For the nonlinear flutter of isotropic plates, Dowell [3,4] used the direct numerical integration approach and determined that six NMs are required to obtain the converged limit-cycle oscillation (LCO). For the flutter of a cantilever plate, Ye and Dowell [5] employed a Rayleigh–Ritz approach with the direct numerical integration. They found that the length-to-width ratio of the cantilever plate was a significant factor on flutter vibration. Harmonic balance is another analytical method, which needs less computational time than direct integration, but it is extremely tedious to implement. Kuo et al. [6], Yuen and Lau [7], and Eastep and MacIntosh [8] applied this method in their studies. The perturbation method is another method adopted by Kuo et al. [6] and Morino [9].

All of the classical studies in nonlinear panel flutter have one limitation: they are only applicable to isotropic or orthotropic rectangular plates with simple boundary conditions. The finite element method coupled with a frequency domain eigensolution was first successfully applied to study linear panel flutter by Olson [10,11]. Liaw and Yang [12] used a 48-degree-of-freedom (DOF) high-order rectangular element and investigated the structural uncertainties on nonlinear supersonic flutter of laminated composite plates. Han and Yang [13] employed a 54-DOF high-order triangular plate element to study the nonlinear panel flutter of rectangular plates. Dixon and Mei [14] studied the nonlinear flutter of rectangular composite panels. The LCO response was obtained using an extended 24-DOF Bogner–Fox–Schmit (BFS) rectangular plate element and a linearized updated mode with nonlinear time function (LUM/NTF) approximate solution procedure. They found that coalescence may occur between the eigenvalues of the first and third NMs, rather than the lowest two modes, for some composite laminates. The LUM/NTF solution procedure in frequency domain was developed by Gray [15]. Xue [16] applied the discrete Kirchhoff theory (DKT) triangular plate element to study nonlinear panel flutter with nonuniform temperature effects. Abdel-Motagaly et al. [17] employed the extended 15-DOF, 3-node Mindlin triangular plate element (MIN3) and studied composite panels subjected to the combined aerodynamic and acoustic pressures.

Flow yaw angle is another issue in flutter analysis. It is known that a minimum of six (or 6×1) in vacuo NMs is required for converged LCO of simply supported isotropic rectangular plates at supersonic flow at zero yaw angle [3,16]. It is then expected that 6×6 (or 36) NMs are needed for isotropic rectangular plates for converged LCO at an arbitrary yawed supersonic flow [18]. Few investigations on LCO have dealt with yawed airflow. Friedmann and Hanin [19] were the first to study nonlinear flutter of simply supported rectangular isotropic and orthotropic panels with arbitrary supersonic yaw directions. They used the first-order quasi-steady aerodynamic theory and Galerkin's method with 4×2 (or eight) NMs (four in the x direction and two in the y direction). Then numerical integration was employed to obtain the LCO response. Chandiramani et al. [20,21] used the third-order piston theory aerodynamics and the higher-order shear deformation theory and investigated nonperiodic flutter of a buckled composite plate. The yawing of flow was considered, and Galerkin's method with a 2×2 (or four) NMs model was employed for simply supported rectangular composite panel. The numerical integration was used for quasi-periodic/chaotic flutter motion. For arbitrary laminated anisotropic composite rectangular plates, Abdel-Motagaly et al. [18] showed that 36 or less NMs of the lowest natural frequencies are needed for accurate LCO, even at zero yaw angle. The LUM/NTF iterative eigensolution procedure developed earlier for system equations in structural-node DOF was extended for the determination of LCO from the system equations in NMs. Modal participation value was introduced for the selection of those NMs contributing the most to LCO. For nonlinear flutter controller design [22,23], dealing with such a large number of NMs would certainly encounter many difficulties. This leads to the motivation for investigating whether it is possible to analyze nonlinear panel flutter as the other reduced basis with fewer number of DOF, particularly, much fewer than the accepted number of NMs. This was recently accomplished by Guo and Mei [24,25] with the introduction of a new class of multidisciplinary aeroelastic modes (AEMs) for the multidisciplinary nonlinear supersonic flutter response. Their results showed that by using AEMs, the number of modal equations could be drastically reduced with little loss in accuracy compared with those using the NMs. And this new class of multidisciplinary AEMs will be employed and extended for the first time to the suppression of flutter of SMA-embedded plates at arbitrary yawed angle and elevated temperatures.

Thermal effects and in-plane loads also play important roles in flutter response. Houbolt [26] was the first to study the buckling stability and flutter boundaries for 2-D panels with uniform temperature distribution. Two linear modes were used for the thermal postbuckling deflection. Dowell [3,4] found that the critical dynamic pressure was reduced and chaotic oscillation might occur with the presence of temperature by establishing four stability regions in the temperature–dynamic pressure (ΔT–λ) plot. The stability regions include four types of panel behaviors: static flat and stable, aerothermally buckled but dynamically stable, LCO, and chaos. Xue and Mei [27] studied the nonuniform temperature effects on the 2-D and 3-D isotropic panels of arbitrary shapes using the DKT element. Yuen and Lau [7] studied the effect of in-plane load on the nonlinear panel flutter using an incremental harmonic balance method. They stated that several LCO at a certain dynamic pressure were possible for a moderately high postbuckling load. Liaw [28] used a 48-DOF rectangular thin-plate finite element to study nonlinear panel flutter under sinusoidal temperature distributions. Zhou [29] transformed the finite element system dynamic equations from the structural-node DOF to modal amplitudes of NMs with temperature effects, and the results agreed very well with the classical PDE/Galerkin method.

Shape memory alloy (SMA) is a special type of metallic alloy that demonstrates the ability to return to some previously defined shape when subjected to an appropriate thermal procedure. These materials can even be plastically deformed at some relatively low temperature, and upon exposure to some higher temperature, they will return to their original shape. An innovative concept is to use the large recovery stress by embedding the prestrained SMA in a fiber-reinforced laminated composite plate, which is called SMA hybrid composites (SMAHC). When the prestrained SMA fibers are heated above the austenite start temperature (A_s), the fibers tend to return to their original or memorized length. Because the fibers are restrained due to the composite matrix (traditional fiber-reinforced composites), the SMA fibers generate large tensile (recovery) stresses. Rogers et al. [30] studied the active strain energy tuning of plates using the large recovery stresses of SMA fibers. Active modal modification was achieved by using stiffness shifting of SMA during temperature activation. Rogers et al. [31] also studied the structural acoustic control using SMA. Duan et al. [32] studied the frequency tuning of the SMAHC plates at elevated temperatures. The results showed that the natural frequencies of SMAHC plates increased greatly, compared with the traditional composite plates without SMA.

Lee and Choi [33] and Lee et al. [34] studied the thermal buckling and postbuckling of composite beams and shells with embedded SMA actuators, respectively. Based on the 1-D thermomechanical constitutive equation of SMA actuators, a simple formula was suggested to calculate the critical buckling temperature of a beam once the SMA actuator is activated [33]. The constitutive equation of

SMA was also incorporated into a finite element model as an ABAQUS subroutine to determine the thermal postbuckling lateral deflections of the beam, plate, and shell structures. The results showed an increased critical buckling temperature and reduced lateral deflection. However, the recovery stresses calculated from the theoretical constitutive equations are very different from the experimental data.

Suzuki and Degaki [35] studied the suppression of supersonic flutter using a SMA in which an SMA plate was attached on an aluminum base plate. It was demonstrated that the critical dynamic pressure could be greatly increased. Tawfik et al. [36] investigated the stability regions for the supersonic flutter of SMAHC plates with various SMA volume fractions and prestrain levels. An enlarged static flat and stable region was achieved.

In this paper, nonlinear supersonic flutter of SMAHC plates with thermal effects are investigated. The approach to deal with SMA nonlinear material properties is based on the strain due to thermal expansion being a cumulative physical quantity, whereas the stress is an instant one. Therefore, the thermal strain is an integral quantity with respect to temperature [37], whereas stress is evaluated with the instant elastic modulus at certain temperatures in the thermoelastic stress–strain relations. Therefore, the present approach does not need the many small temperature increments as in the marching method [32]. The integral approach is suitable for any nonlinear temperature-dependent (TD) material properties, which is naturally considered in the integral formulation of calculating strain. Experimental data of SMA recovery stress are employed in the stress–strain relation of a SMAHC lamina to avoid any error caused by an approximate mathematical model. The thermal loads are considered in the finite element model because SMA needs temperature increase to be activated. This paper contributes the first attempt to transfer the finite element system equations of motion in structural-nodal DOF to aeroelastic modal coordinates, to reduce the number of DOF for the suppression of flutter using SMA. The time-domain numerical integration method is employed to determine the time history of flutter response. Potential composites suitable for high-temperature SMAHC applications such as some advanced thermoplastics: polyetheretherketone (PEEK) and polyphenylene sulfide (PPS) can be used in the temperature range up to 600–700°F (315–370°C). In the present paper, graphite–epoxy (Gr–Ep) composite panels with or without SMA are investigated. The use of graphite–epoxy in this paper is for demonstration of the advantages of using SMA in suppression of flutter. Results show that for composite panels embedded with SMA, the desired flat and stable region can be raised large enough and flutter can be suppressed by the proper selection of SMA volume fraction and prestrain for supersonic aerospace applications.

Finite Element Formulation

Constitutive Equations

The thermoelastic stress–strain relation for a kth SMAHC lamina can be derived and expressed as [36,37]

$$\{\sigma\}_k = \begin{Bmatrix} \sigma_x \\ \sigma_y \\ \tau_{xy} \end{Bmatrix}_k = [\bar{Q}]_k \left(\{\varepsilon\} - \int_{T_{\text{ref}}}^{T} \{\alpha(\tau)\}_k \, \mathrm{d}\tau \right) \qquad T < A_s$$

$$= [\bar{Q}]_k \{\varepsilon\} + \{\sigma_r\}_k v_{sk} - ([\bar{Q}]_m v_m)_k \int_{T_{\text{ref}}}^{T} (\{\alpha(\tau)\}_m)_k \, \mathrm{d}\tau \qquad T \geq A_s \tag{1}$$

where $[\bar{Q}]$ and $[\bar{Q}]_m$ denote the transformed reduced-stiffness matrices of the SMA-embedded lamina ($v_s \neq 0$) and the matrix ($v_s = 0$). It is noted that the matrix properties are also temperature-dependent (see Table 1). The material stiffness matrices $[\bar{Q}]$ and $[\bar{Q}]_m$ are, therefore, temperature-dependent. It is worth noting that nonlinear thermal strain is inherently cumulative and thus an integral is employed. The formulation shows that the SMA-embedded composite lamina behaves as a regular one before the SMA is activated (i.e., at temperature $T < A_s$); an extra stress term is added to account for the recovery stress after SMA is activated (i.e., at $T > A_s$).

It is assumed that the panel is thin and the rotary inertia and transverse shear deformation effects are thus negligible. The in-plane strains $\{\varepsilon^o\}$ and curvatures $\{\kappa\}$ based on von Kármán large deflection and classical laminated plate theories are given by [14,18]

$$\{\varepsilon\} = \begin{Bmatrix} u_{,x} \\ v_{,y} \\ u_{,y} + v_{,x} \end{Bmatrix} + \frac{1}{2} \begin{Bmatrix} w_{,x}^2 \\ w_{,y}^2 \\ 2w_{,x}\, w_{,y} \end{Bmatrix} + z \begin{Bmatrix} -w_{,xx} \\ -w_{,yy} \\ -2w_{,xy} \end{Bmatrix} = \begin{Bmatrix} \varepsilon_m^0 \end{Bmatrix} + \begin{Bmatrix} \varepsilon_b^0 \end{Bmatrix} + z\{\kappa\} = \{\varepsilon^0\} + z\{\kappa\} \tag{2}$$

The stress resultants per unit length of the SMA-embedded composite plate are thus given as

$$\begin{Bmatrix} N \\ M \end{Bmatrix} = \begin{bmatrix} A & B \\ B & D \end{bmatrix} \begin{Bmatrix} \varepsilon^o \\ \kappa \end{Bmatrix} + \begin{Bmatrix} N_r \\ M_r \end{Bmatrix} - \begin{Bmatrix} N_{\Delta T} \\ M_{\Delta T} \end{Bmatrix} \tag{3}$$

where the laminate stiffness matrices and stress resultants are also temperature-dependent and they are

$$([A], [B], [D]) = \int_{-h/2}^{h/2} [\bar{Q}]_k (1, z, z^2) \, \mathrm{d}z \tag{4}$$

$$(\{N\}, \{M\}) = \int_{-h/2}^{h/2} \{\sigma\}_k (1, z) \, \mathrm{d}z \tag{5}$$

$$(\{N_r\}, \{M_r\}) = 0 \qquad T < A_s$$

$$= \int_{-h/2}^{h/2} \{\sigma_r\}_k v_{sk} (1, z) \, \mathrm{d}z \qquad T \geq A_s \tag{6}$$

$$\begin{aligned}(\{N_{\Delta T}\},\{M_{\Delta T}\}) &= \int_{-h/2}^{h/2}\left[[\bar{Q}]_k \int_{T_{\text{ref}}}^{T}\{\alpha(\tau)\}_k \,\mathrm{d}\tau\right](1,z)\,\mathrm{d}z \qquad T < A_s \\ &= \int_{-h/2}^{h/2}\left[([\bar{Q}]_m v_m)_k \int_{T_{\text{ref}}}^{T}(\{\alpha(\tau)\}_m)_k \,\mathrm{d}\tau\right](1,z)\,\mathrm{d}z \qquad T \geq A_s\end{aligned} \tag{7}$$

Supersonic Aerodynamic Theory for Panel Flutter

Quasi-steady first-order piston theory is a verified aerodynamic model [1] that has been successfully applied to many panel flutter studies. This theory describes the aerodynamic pressure on a skin panel of a flight vehicle at supersonic speed. The theory is based on the assumptions that

1) The local motion of the panel acts as a piston.
2) The air is ideal and it has a constant specific heat; the process of the airflow is isentropic.
3) The local panel motion velocity is much smaller than the airflow velocity.
4) The airflow is parallel to the panel surface.
5) The effect of any air entrapped below the panel (cavity) is neglected.

The piston theory cannot predict aerodynamic heating. The present study is a simple qualitative evaluation aimed at determining the effectiveness of SMA in suppression of flutter. In a realistic model, however, one may need to use the Navier–Stokes equations to obtain the more accurate aerodynamic loading in the presence of heat transfer.

The first-order piston theory considering flow yaw angle is

$$P_a = -\frac{2q}{\beta}\left[\frac{\partial w}{\partial x}\cos\Lambda + \frac{\partial w}{\partial y}\sin\Lambda + \frac{M_\infty^2 - 2}{M_\infty^2 - 1}\frac{1}{V}\frac{\partial w}{\partial t}\right] \tag{8}$$

where $\beta = \sqrt{M_\infty^2 - 1}$, and w is the panel transverse displacement. Equation (8) can also be written as

$$P_a = -\left[\lambda\frac{D_{110}}{a^3}\left(\frac{\partial w}{\partial x}\cos\Lambda + \frac{\partial w}{\partial y}\sin\Lambda\right) + \frac{g_a}{\omega_o}\frac{D_{110}}{a^4}\frac{\partial w}{\partial t}\right] \tag{9}$$

where D_{110} is the first element in the laminate bending stiffness matrix $[D]$, calculated when all of the fibers of the SMAHC plate are aligned in the x direction and

$$\lambda = \frac{2qa^3}{\beta D_{110}}, \qquad \mu = \frac{\rho_a a}{\rho h}, \qquad C_a = \left(\frac{M_\infty^2 - 2}{M_\infty^2 - 1}\right)^2\frac{\mu}{\beta}, \qquad g_a = \frac{\rho_a V(M_\infty^2 - 2)}{\beta^3\rho h\omega_o} = \sqrt{\lambda C_a}, \qquad \omega_o = \sqrt{\frac{D_{110}}{\rho h a^4}} \tag{10}$$

In an SMAHC panel, the values of ρ, D_{110}, and ω_o will change with different volume fraction of SMA. The parameters ρ, D_{110}, and ω_o serve only to transfer the coefficients in Eq. (8) into nondimensional ones. For the purpose of comparison, dynamic pressure should be consistent for plates with or without SMA. Therefore, the adopted parameters ρ, D_{110}, and ω_o are defined corresponding to the traditional composite plate without SMA ($v_s = 0$) in the present study.

With the application of the variational principle and the kinematic boundary conditions, the governing equation using finite element method for an SMAHC plate undergoing large deflection subjected to a temperature increase $\Delta T = T - T_{\text{ref}}$ can be written [25,32] as

$$\begin{aligned}&\begin{bmatrix} M_b & 0 \\ 0 & M_m \end{bmatrix}\begin{Bmatrix} \ddot{W}_b \\ \ddot{W}_m \end{Bmatrix} + \begin{bmatrix} G(\lambda, C_a) & 0 \\ 0 & 0 \end{bmatrix}\begin{Bmatrix} \dot{W}_b \\ \dot{W}_m \end{Bmatrix} + \left(\lambda\begin{bmatrix} A_a(\Lambda) & 0 \\ 0 & 0 \end{bmatrix} + \begin{bmatrix} K_b & K_{bm} \\ K_{mb} & K_m \end{bmatrix} - \begin{bmatrix} K_{\Delta Tb} & 0 \\ 0 & 0 \end{bmatrix} + \begin{bmatrix} K_{rb} & 0 \\ 0 & 0 \end{bmatrix}\right)\begin{Bmatrix} W_b \\ W_m \end{Bmatrix} \\ &+ \left(\begin{bmatrix} K1_{Nm}(W_m) + K1_{NB}(W_b) & K1_{bm}(W_b) \\ K1_{mb}(W_b) & 0 \end{bmatrix} + \begin{bmatrix} K2_b(W_b^2) & 0 \\ 0 & 0 \end{bmatrix}\right)\begin{Bmatrix} W_b \\ W_m \end{Bmatrix} = \begin{Bmatrix} P_{b\Delta T} \\ P_{m\Delta T} \end{Bmatrix} - \begin{Bmatrix} P_{br} \\ P_{mr} \end{Bmatrix}\end{aligned} \tag{11a}$$

or simply

$$\begin{aligned}&[M]\{\ddot{W}\} + [G(\lambda, C_a)]\{\dot{W}\} + (\lambda[A_a(\Lambda)] + [K] - [K_{N\Delta T}] \\ &\quad + [K_r])\{W\} + ([K1(W)] + [K2(W^2)])\{W\} = \{P_{\Delta T}\} - \{P_r\}\end{aligned} \tag{11b}$$

where the geometrical stiffness matrices $[K_{N\Delta T}]$ and $[K_r]$ are due to thermal in-plane force $\{N_{\Delta T}\}$ and SMA recovery in-plane force $\{N_r\}$, respectively; and the subscripts mb (bm), Nm, and NB indicate that the corresponding stiffness matrix or load vector is dependent on laminate coupling stiffness $[B]$, in-plane force components $\{N_m\} = ([A]\{\varepsilon_m^o\})$, and $\{N_B\} = ([B]\{\kappa\})$, respectively. Note that the system Eq. (11) is applicable for an arbitrary stacking of composite lamina. It can be either symmetric or asymmetric.

The number of structural-node DOF in modeling a typical plate is usually in the hundreds, and in addition, the linear stiffness matrices $[K]$, $[K_{N\Delta T}]$, and $[K_r]$ and the nonlinear stiffness matrices $[K1]$ and $[K2]$ are all temperature-dependent. Thus, the dynamic numerical analysis is computationally intense and costly. Therefore, Eq. (11) needs to be transformed to the reduced modal coordinates. Neglecting the in-plane inertia due to higher frequencies, the in-plane displacement vector $\{W_m\}$ can be expressed from the second equation of Eq. (11a) into a function of bending displacement vector $\{W_b\}$ as

$$\begin{aligned}\{W_m\} &= [K_m]^{-1}(\{P_{m\Delta T}\} - \{P_{mr}\}) - [K_m]^{-1}[K_{mb}]\{W_b\} \\ &\quad - [K_m]^{-1}[K1_{mb}(W_b)]\{W_b\} = \{W_m\}_0 - \{W_m\}_1 - \{W_m\}_2\end{aligned} \tag{12}$$

where the three in-plane displacement components $\{W_m\}_0$, $\{W_m\}_1$, and $\{W_m\}_2$ denote that $\{W_m\}$ is a combined zero-, first-, and second-order function of $\{W_b\}$.

Table 1 Material properties of nitinol and Gr–Ep composite lamina

Nitinol		Graphite–epoxy	
See Figs. 2 and 3 for Young's modulus and recovery stresses		E_1	$22.5 \times 10^6(1 - 3.53 \times 10^{-4} \cdot \Delta T)$ psi $[155(1 - 6.35 \times 10^{-4} \cdot \Delta T)$ GPa]
G	3.604×10^6 psi (24.9 GPa), $T < A_s$	E_2	$1.17 \times 10^6(1 - 4.27 \times 10^{-4} \cdot \Delta T)$ psi $[8.07(1 - 7.69 \times 10^{-4} \cdot \Delta T)$ GPa]
	3.712×10^6 psi (25.6 GPa), $T \geq A_s$	G_{12}	$0.66 \times 10^6(1 - 6.06 \times 10^{-4} \cdot \Delta T)$ psi $[4.55(1 - 1.09 \times 10^{-3} \cdot \Delta T)$ GPa]
ρ	0.6067×10^{-3} lb-s^2/in.^{4} (6450 kg/m^3)	ρ	0.1458×10^{-3} lb-s^2/in.^{4} (1550 kg/m^3)
μ	0.3	μ_{12}	0.22
α	5.7×10^{-6}/°F$(10.26 \times 10^{-6}$/°C)	α_1	$-0.04 \times 10^{-6}(1 - 1.25 \times 10^{-3} \cdot \Delta T)$/°F $[-0.07 \times 10^{-6}(1 - 0.69 \times 10^{-3} \cdot \Delta T)$/°C]
		α_2	$16.7 \times 10^{-6}(1 + 0.41 \times 10^{-4} \cdot \Delta T)$/°F $[30.0 \times 10^{-6}(1 + 0.28 \times 10^{-4} \cdot \Delta T)$/°C]

Substituting Eq. (12) into the first equation of Eq. (11a), it can be condensed into a function of $\{W_b\}$ only as

$$[M_b]\{\ddot{W}_b\} + [G(\lambda, C_a)]\{\dot{W}_b\} + (\lambda[A_a(\Lambda)] + [K_{\text{lin}}] + [K_1] + [K_2])\{W_b\} = \{P_b\} \tag{13}$$

where

$$\begin{aligned}
[K_{\text{lin}}] &= [K_b] - [K_{\Delta Tb}] + [K_{rb}] - [K_{bm}][K_m]^{-1}[K_{mb}] \\
&\quad + 2[K1_{Nm}(\{W_m\}_0)] \\
[K_1] &= [K1_{NB}] - [K1_{Nm}(\{W_m\}_1)] - [K1_{bm}][K_m]^{-1}[K_{mb}] \\
&\quad - [K_{bm}][K_m]^{-1}[K1_{mb}] \\
[K_2] &= [K2_b] - [K1_{bm}][K_m]^{-1}[K1_{mb}] - [K2_{Nm}(\{W_m\}_2)] \\
\{P_b\} &= \{P_{b\Delta T}\} - \{P_{br}\} - [K_{bm}]\{W_m\}_0
\end{aligned} \tag{14}$$

Next, the bending displacement vector $\{W_b\}$ can be expressed as a linear summation of the product of aeroelastic modal amplitudes $q_r(t)$ and some known AEMs [24,25] $\{\phi_r\}$ as

$$\{W_b\} \approx \sum_{r=1}^{n} q_r(t)\{\phi_r\} = [\Phi]\{q\} \tag{15}$$

where $\{\phi_r\}$ is determined by solving the eigenvalue problem of the linear free vibration of the prethermally loaded system (i.e., at reference temperature) as

$$\omega_r^2[M_b]\{\phi_r\} = (\lambda_o[A_a(\Lambda)] + [K_b] - [K_{bm}][K_m]^{-1}[K_{mb}])\{\phi_r\} \tag{16}$$

The λ_o is a certain selected dynamic pressure value, and the selection of λ_o is described in [24]. The aerodynamic matrix $[A_a]$ is skew-symmetric and thus the combined matrix $(\lambda_o[A_a] + [K_b] - [K_{bm}][K_m]^{-1}[K_{mb}])$ is asymmetric. Hence, the desirable properties of the eigenvalues and eigenvectors associated with symmetric matrices no longer exist. In particular, for $\lambda_o < \lambda_{\text{cr}}$, the eigenvalues and eigenvectors are real, but the eigenvectors are no longer orthogonal. The right and left eigenvectors [24] are employed here to transform the system equations in structural-node DOF into aeroelastic modal coordinates.

Equation (13) is then transformed into aeroelastic modal coordinates as

$$[\bar{M}_b]\{\ddot{q}\} + [\bar{G}]\{\dot{q}\} + (\lambda[\bar{A}_a] + [\bar{K}] + [\bar{K}_q] + [\bar{K}_{qq}])\{q\} = \{\bar{P}_b\} \tag{17}$$

where the modal mass, modal aerodynamic damping, modal influence, and modal linear stiffness matrices are given by

$$([\bar{M}_b], [\bar{G}], [\bar{A}_a], [\bar{K}]) = [\Phi_L]^T([M_b], [G], [A_a], [K_{\text{lin}}])[\Phi] \tag{18}$$

The first-order and second-order nonlinear modal stiffness matrices $[\bar{K}_q]$ and $[\bar{K}_{qq}]$ and modal force vectors $\{\bar{P}_b\}$ are

$$\begin{aligned}
[\bar{K}_q] &= [\Phi_L]^T \sum_{r=1}^{n} q_r([K1_{NB}]^{(r)} - [K1_{Nm}]^{(r)} \\
&\quad - [K1_{bm}]^{(r)}[K_m]^{-1}[K_{mb}] - [K_{bm}][K_m]^{-1}[K1_{mb}]^{(r)})[\Phi]
\end{aligned} \tag{19}$$

$$\begin{aligned}
[\bar{K}_{qq}] &= [\Phi_L]^T \sum_{r=1}^{n}\sum_{s=1}^{n} q_r q_s \\
&\quad \times ([K2_b]^{(rs)} - [K2_{Nm}]^{(rs)} - [K1_{bm}]^{(r)}[K_m]^{-1}[K1_{mb}]^{(s)})[\Phi]
\end{aligned} \tag{20}$$

$$\{\bar{P}_b\} = [\Phi_L]^T\{P_b\} \tag{21}$$

where $[\Phi_L]$ is the matrix of left eigenvectors corresponding to the selected AEMs, which are the selected right eigenvectors. Because the original whole square matrix of left eigenvectors $[\Phi'_L]$ is related with the original whole square matrix of right eigenvectors $[\Phi']$ by $[\Phi'_L]^T = [\Phi']^{-1}$, $[\Phi_L]$ is obtained by extracting the corresponding parts from the $[\Phi']^{-1}$. And again, the modal stiffness matrices $[\bar{K}]$, $[\bar{K}_q]$, and $[\bar{K}_{qq}]$ are temperature-dependent.

A participation value, which evaluates the contribution from the rth mode to the total response, is defined as

$$P(r\text{th mode}) = \frac{\max|q_r|}{\sum_{s=1}^{n}(\max|q_s|)} \tag{22}$$

Thus, the minimum number of AEMs for an accurate and converged solution can be determined based on the modal participation values. Time numerical integration is employed to determine the time history of aeroelastic modal amplitudes from Eq. (17). Once the modal coordinate vector $\{q\}$ is obtained, the displacement vectors $\{W_m\}$ and $\{W_b\}$ can be determined using Eqs. (12) and (15), respectively.

Equation (17) is also applicable for static loads (e.g., for static aerothermal buckling analysis). In this case, by simply dropping the inertial and damping terms, Eq. (17) becomes

$$(\lambda[\bar{A}_a] + [\bar{K}] + [\bar{K}_q] + [\bar{K}_{qq}])\{q\} = \{\bar{P}_b\} \tag{23}$$

Equation (23) is a set of nonlinear algebraic equations and the Newton–Raphson iteration method is employed to determine the static response of $\{q\}$.

Results and Discussion

Validation

To validate the present aeroelastic modal formulation, the LCO results are determined and compared with results using classical NM method for a simply supported aluminum square plate at a zero flow angle ($\Lambda = 0$ deg). The BFS C^1 conforming rectangular plate element [38] is employed. The BFS element has 24 DOF, 6 at each node: the bending DOF $\{w_b\}$, comprising transverse displacements w and the first and second derivatives of displacements $w_{,x}$, $w_{,y}$, and $w_{,xy}$; and the in-plane DOF $\{w_m\}$, comprising u and v.

For the simply supported isotropic square plate, it is known that $\lambda_{\text{cr}} = 512$ [3]. In Fig. 1, the LCO amplitudes using two AEMs ($\lambda_o = 510$) are determined and compared with results using six NMs and those from Dowell [3]. The present modal formulation using two AEMs gives very accurate LCO response. The readers are referred to additional validation of the application of AEMs for flutter responses [24,25].

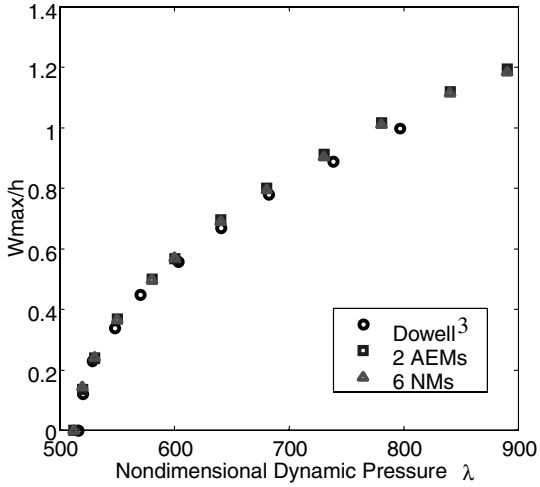

Fig. 1 Comparison of LCO amplitudes between Dowell [3] and finite element modal method using two AEMs and six NMs for a simply supported isotropic square plate at $\Lambda = 0$ deg.

Problem Description

The panel flutter response is investigated and displayed in the ΔT–λ domain due to combined thermal and aerodynamic loads. The results determined for the SMAHC plates are compared with those of traditional composite plates. For the purpose of comparison, a rectangular traditional composite plate and the SMAHC plates studied here have the identical dimensions, laminations, and composite matrix. The plate dimension is $15 \times 12 \times 0.05$ in. ($38.1 \times 30.5 \times 0.13$ cm), the lamination is eight-layered with a stacking sequence $[0/-45/45/90]_s$, and the composition is Gr–Ep. Nitinol [39] is chosen as the SMA fibers embedded in the Gr–Ep plate. The nitinol fibers are embedded in all eight layers and are along the same direction as the graphite fibers due to manufacturing restrictions. Young's modulus vs temperature and recovery stresses vs temperature of nitinol are from Cross et al. , as shown in Figs. 2 and 3. The phase transformation is activated at the reference temperature 70°F. The other properties of nitinol are given in Table 1. The material properties of Gr–Ep are also considered as temperature-dependent, as shown in Table 1. The boundary conditions are all clamped with immovable in-plane edges $u(0, y) = u(a, y) = v(x, 0) = v(x, b) = 0$. The full plate is modeled with 12×12 mesh or 144 BFS elements for both $\Lambda = 0$ deg and $\Lambda \neq 0$ deg.

Thermal Buckling

The postbuckling deflections of SMAHC plates can be obtained by neglecting the dynamic parts in Eq. (11), that is,

$$([K] - [K_{N\Delta T}] + [K_r])\{W\} + ([K1(W)] + [K2(W^2)])\{W\} = \{P_{\Delta T}\} - \{P_r\} \tag{24}$$

The thermal deflections of the plates with and without SMA are then calculated by applying the Newton–Raphson method and are shown in Fig. 4. It is demonstrated that the critical temperature increases greatly for the SMAHC plates, which is $\Delta T_{\text{cr}} = 245$°F for ($v_s = 10\%$, $\varepsilon_r = 3\%$), 360°F for SMAHC ($v_s = 10\%$, $\varepsilon_r = 5\%$), compared with 40°F for the traditional composite plate. In other words, the recovery stress from the embedded SMA enlarges the desired buckling-free temperature range. Skin panels of the QSP could reach 350°F at cruise (Mach 2.2–2.4). The results indicate that the clamped composite plates embedded with SMA ($v_s = 10\%$, $\varepsilon_r = 5\%$) are applicable to QSP application for their capability to eliminate the large thermal deflection completely.

Traditional Composite Plates Without SMA-Embedding

It is found that six AEMs ($\lambda_o = 464$) will give accurate and converged aerothermal deflection and LCO for the traditional $[0/-45/45/90]_s$ composite plate, as shown in Fig. 5 and Table 2. $W_{\max}/h$ vs dynamic pressure is plotted in Fig. 5 for the traditional composite plate at $\Lambda = 0$ deg and $\Delta T = 50$°F ($\Delta T/\Delta T_{\text{cr}} = 1.26$) using 25 NMs and 6 AEMs, respectively. The comparison indicates that the result using six AEMs yields excellent agreement with that of 25 NMs (although 25 NMs might not be the minimum number of modes needed, it provides an accurate analysis result to be compared with). This example clearly demonstrates the advantages in computation

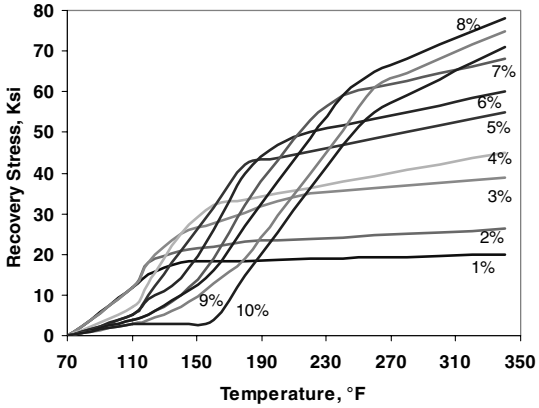

Fig. 2 Nitinol recovery stress at different prestrain [39].

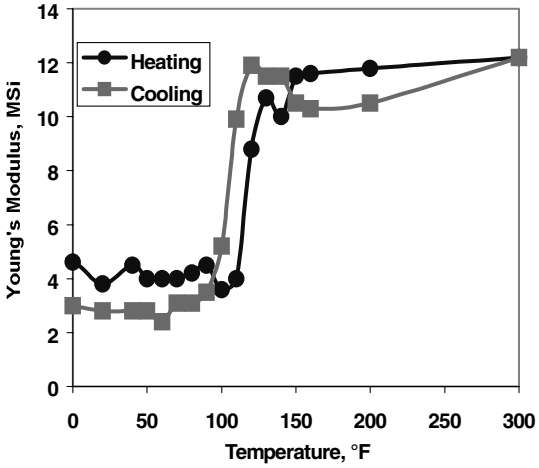

Fig. 3 Nitinol modulus of elasticity [39].

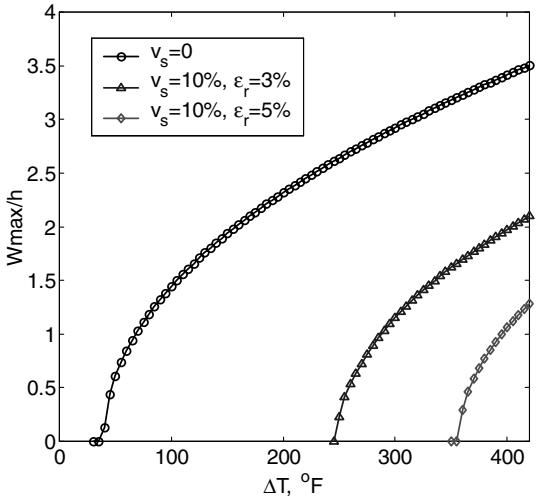

Fig. 4 The thermal buckling deflection $W_{\max}/h$ of a clamped traditional composite plate ($v_s = 0$) and the clamped SMAHC plates ($v_s \neq 0$).

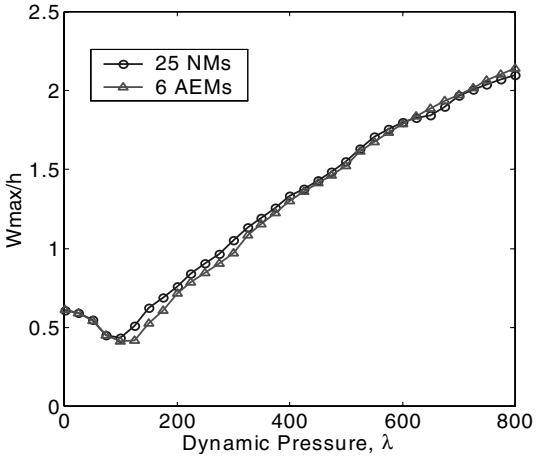

Fig. 5 Comparison of aerothermal deflection and LCO amplitude using 25 NMs and 6 AEMs for a clamped traditional $[0/-45/45/90]_s$ composite plate at $\Delta T = 50°\text{F}$ and $\Lambda = 0\,\text{deg}$.

time and cost in using the much smaller number of AEMs compared with the traditional approach using a much larger number of NMs for flutter analyses. Table 2 shows a fast convergence of solution with very small contributions from higher modes (e.g. the contribution from the fifth and sixth are all less than 2%).

The four types of dynamic motions using six AEMs are shown in Figs. 6–9, represented with time history, phase plot, power spectrum density (PSD) plot, and Poincaré map.

At $\lambda = 500$, $\Lambda = 0\,\text{deg}$, and $\Delta T/\Delta T_{\text{cr}} = 1.0$, as shown in Fig. 6, the closed-phase plot and one dominant frequency in the PSD plot clearly indicate a simple harmonic LCO. There is only one point in the Poincaré map, standing for when the maximum point reaches the local maximum value, the plate center has just one position corresponding to it. This one-to-one correlation indicates simple harmonic motion.

At $\lambda = 275$, $\Lambda = 0\,\text{deg}$, and $\Delta T/\Delta T_{\text{cr}} = 2.0$, the vibration type changes to periodic, as shown in Fig. 7. The phase plot comprises a small orbit about each thermally buckled state and a large orbit. The

Table 2 Modal participations of six AEMs ($\lambda_o = 464$) for a clamped traditional $[0/-45/45/90]_s$ composite plate at $\Lambda = 0\,\text{deg}$ and $\Delta T = 50°\text{F}$

		Modal participation, %					
λ	$W_{\max}/h$	q1	q2	q3	q4	q5	q6
0	0.61	49.68	48.05	1.70	0.19	0.24	0.13
100	0.41	52.41	25.00	11.61	9.27	1.19	0.51
200	0.72	53.54	36.46	4.92	3.57	1.09	0.04
300	0.97	52.76	43.32	1.19	1.97	0.53	0.60
400	1.13	47.76	50.36	1.32	0.30	0.26	0.11
500	1.39	40.53	55.92	0.51	1.61	1.28	1.44
600	1.79	63.42	26.82	3.27	3.71	1.93	0.83
700	1.98	60.11	31.62	2.80	2.66	1.76	1.03
800	2.14	53.93	41.67	2.04	1.50	0.74	0.11

PSD plot indicates three or four dominant frequencies. In general, one point in a Poincaré map expresses the recurrent behavior of a motion, which in turn, stands for a periodic motion.

The plate may also show a more complex periodic motion at $\lambda = 200$, $\Lambda = 0\,\text{deg}$, and $\Delta T/\Delta T_{\text{cr}} = 3.0$, as shown in Fig. 8. At such a combination of high $\Delta T/\Delta T_{\text{cr}}$ and moderate λ, the plate motion evolves from periodic oscillation to quasi-periodic oscillation. The Poincaré map shows a cluster of points gathering in the upper right and lower left section of the plot, indicating that when the maximum point reaches the local maximum position, plate center can vibrate somewhere on a straight line position but shows no recurrence.

At the combination of medium dynamic pressure and high temperature, such as $\lambda = 325$, $\Lambda = 0\,\text{deg}$, and $\Delta T/\Delta T_{\text{cr}} = 4.0$, as shown in Fig. 9, the plate is likely to undergo chaotic oscillation. Compared with quasi-periodic oscillation in Fig. 8, chaos shows diffusion on the phase plot that almost fills the entire region from minima to maxima, and the broadening of power spectrum peaks in the PSD plot. In the Poincaré map, the cluster of points stretches over the entire region from negative and positive, indicating that when the maximum point reaches the local maximum, plate center can vibrate anywhere, which leads to the unpredictability of the motion. The phase plot indistinctly shows the strange attractors at about

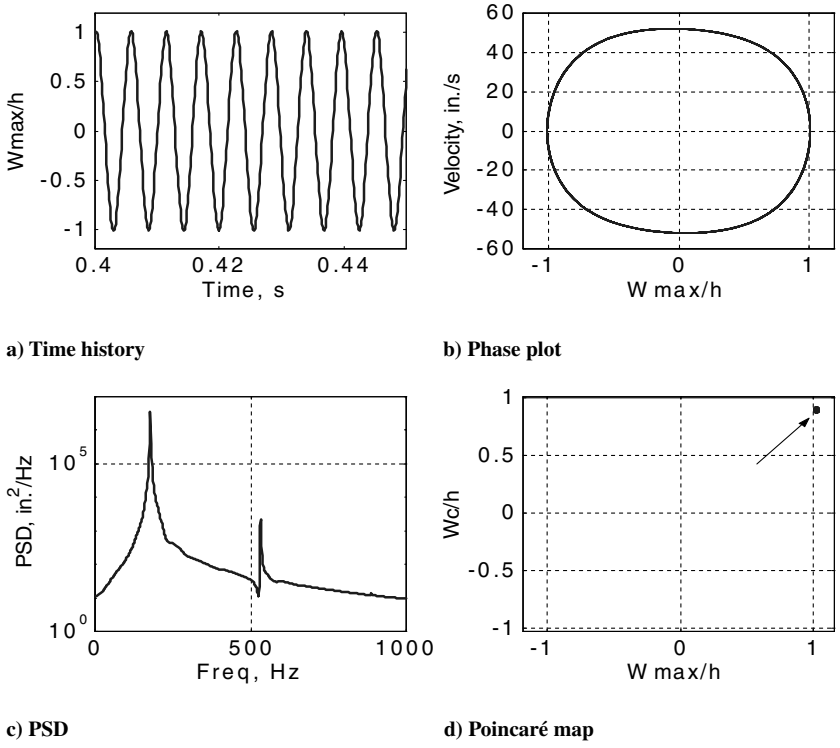

a) Time history **b) Phase plot**

c) PSD **d) Poincaré map**

Fig. 6 Simple harmonic LCO of a clamped traditional $[0/-45/45/90]_s$ composite plate at $\lambda = 500$, $\Lambda = 0\,\text{deg}$, and $\Delta T/\Delta T_{\text{cr}} = 1.0$.

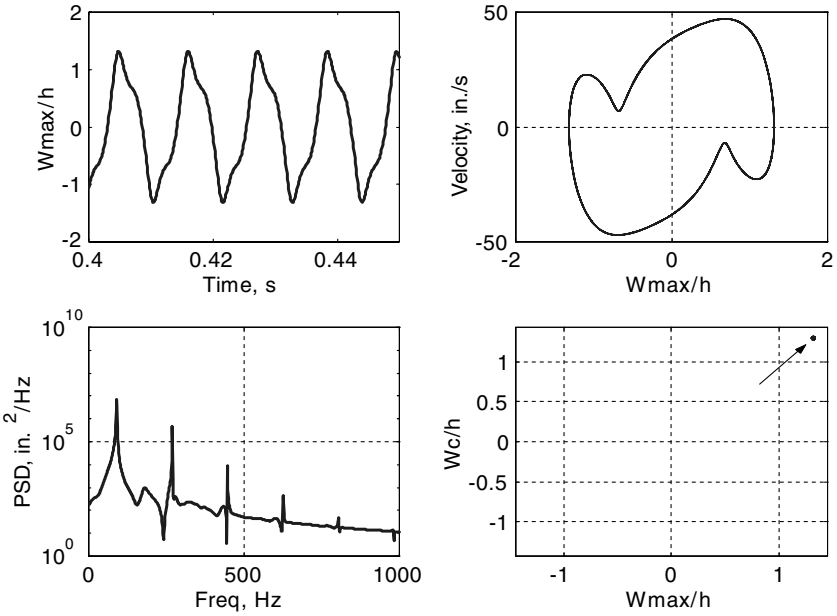

Fig. 7 Periodic LCO of a clamped traditional $[0/-45/45/90]_s$ composite plate at $\lambda = 275$, $\Lambda = 0$ deg, and $\Delta T/\Delta T_{cr} = 2.0$.

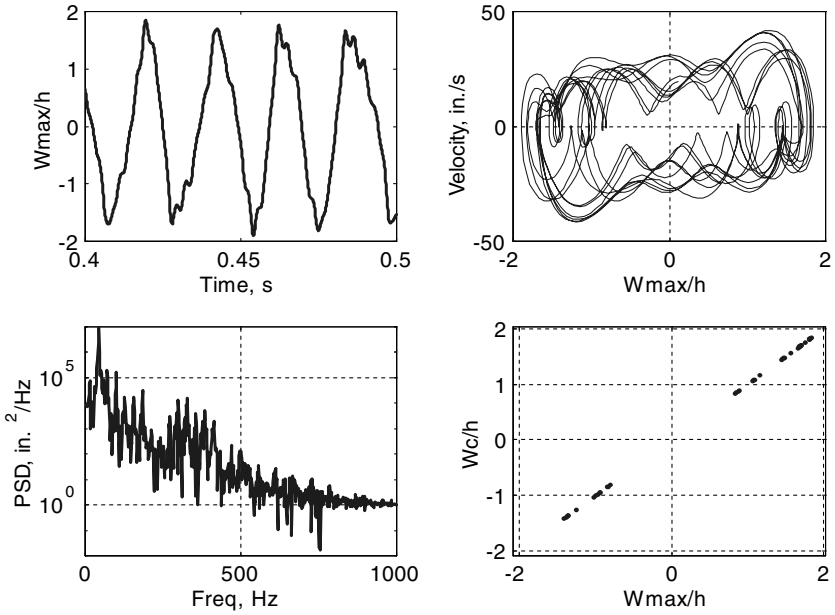

Fig. 8 Quasi-periodic oscillation of a clamped traditional $[0/-45/45/90]_s$ composite plate at $\lambda = 200$, $\Lambda = 0$ deg, and $\Delta T/\Delta T_{cr} = 3.0$.

$W_{max}/h = -1.8$ and 1.8, which is not seen in quasi-periodic oscillation. For a more rigorous confirmation of chaotic motion, the appropriate Lyapunov exponent has to be evaluated.

The plate's aerothermal deflection and LCO amplitude at the maximum point vs dynamic pressure at various temperatures are shown in Fig. 10. The left side curves are the aerothermal deflections, before λ reaches the critical value (λ_{cr}) for flutter. The right side curves are the LCO amplitudes. It is seen that with the increase of λ, aerothermal deflection decreases. The decrease is accredited to the increasing of frequency with the increase of λ. At $\Delta T = 50$°F (also shown in Fig. 5), the aerothermal deflection drops to a minimum value, then the LCO commences from there. At $\Delta T > 50$°F, the plate cannot be blown to flat and begins flutter right after aerothermal buckling [16]. It is noticed that at low temperatures, the LCO amplitudes increase smoothly with the increase of λ. This is where harmonic LCO occurs. As temperature goes up, the irregular motion begins to occur, indicating that the flutter could have quasi-periodic or chaotic motion.

Figure 11 shows the stability regions in the temperature–dynamic pressure (ΔT-λ) domain. There are essentially four regions: flat and stable, buckled but dynamically stable, LCO flutter (including harmonic, periodic, and quasi-periodic motions), and chaos. The boundary between the LCO region and the chaos region is not precisely determined, because this is not the purpose of the present study. The objective is to investigate the enlargement of the flat and stable region using SMA. The periodic and quasi-periodic motions lie between harmonic LCO and chaos. With the increase of ΔT and λ, the nearly simple harmonic LCO has the tendency to evolve to periodic LCO; the periodic region therefore resides in the lower right of LCO region, between LCO and chaos. Figure 11 also shows the

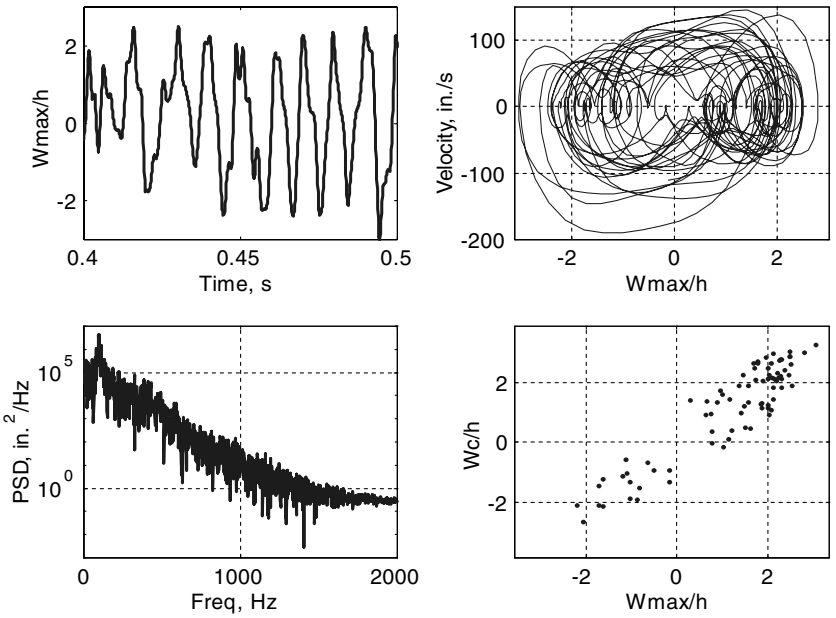

Fig. 9 Chaotic oscillation of a clamped traditional $[0/-45/45/90]_s$ composite plate at $\lambda = 325$, $\Lambda = 0$ deg, and $\Delta T/\Delta T_{cr} = 4.0$.

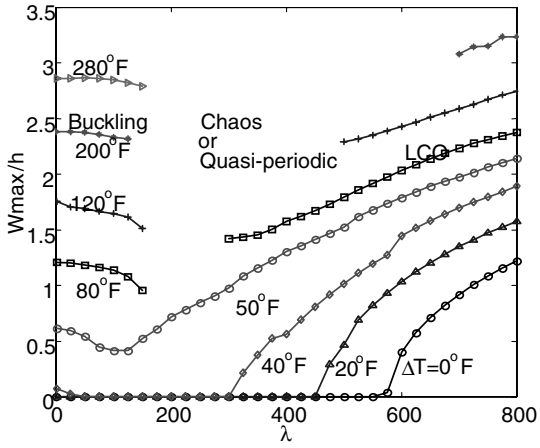

Fig. 10 Aerothermal deflection and LCO amplitude vs dynamic pressure λ of a clamped traditional $[0/-45/45/90]_s$ composite plate at $\Lambda = 0$ deg.

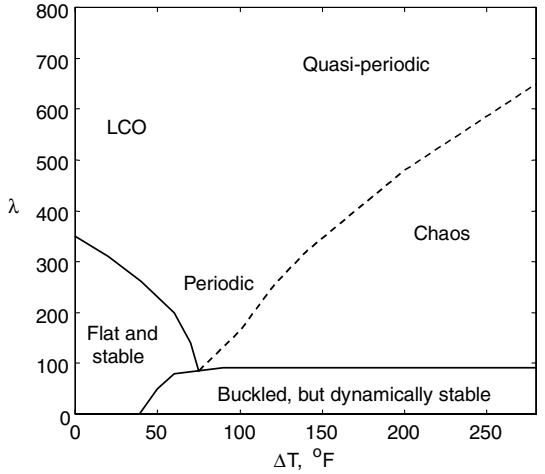

Fig. 12 Stability regions in ΔT–λ domain of the clamped traditional $[0/-45/45/90]_s$ composite plate at $\Lambda = 45$ deg.

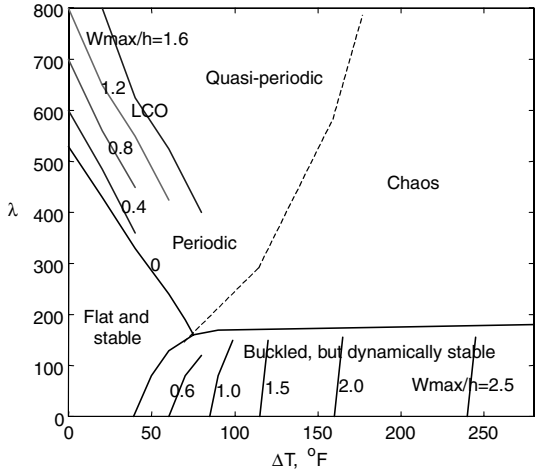

Fig. 11 Stability regions in ΔT–λ domain of the clamped traditional $[0/-45/45/90]_s$ composite plate at $\Lambda = 0$ deg.

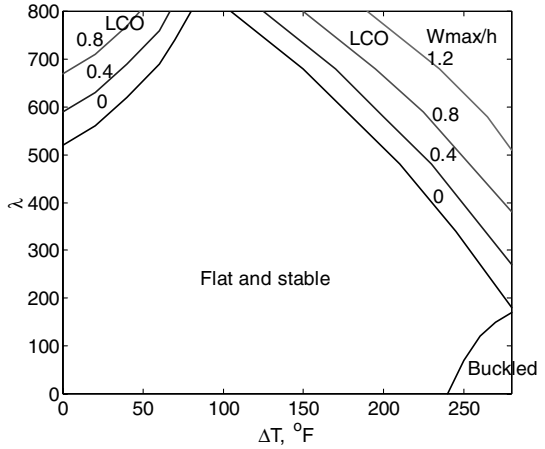

Fig. 13 Stability regions in ΔT–λ domain of the clamped SMAHC ($v_s = 10\%$ and $\varepsilon_r = 3\%$) plate at $\Lambda = 0$ deg.

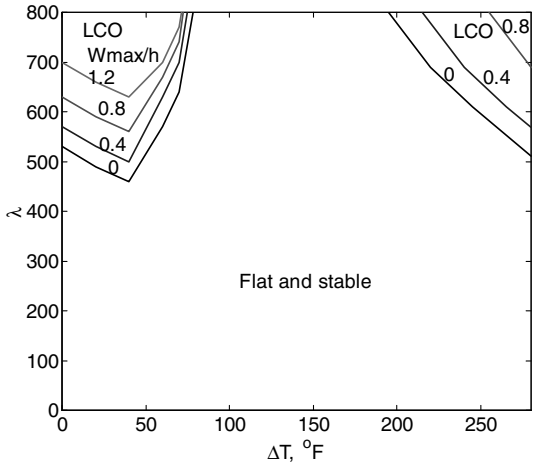

Fig. 14 W_{max}/h vs dynamic pressure and temperature of a clamped SMAHC ($v_s = 10\%$ and $\varepsilon_r = 5\%$) plate at $\Lambda = 0$ deg.

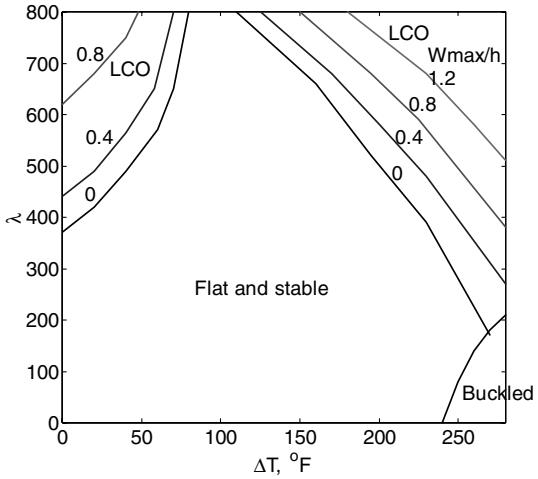

Fig. 15 W_{max}/h vs dynamic pressure and temperature of a clamped SMAHC ($v_s = 10\%$ and $\varepsilon_r = 3\%$) plate at $\Lambda = 45$ deg.

lines inside the LCO region in which the flutters have the same amplitudes and the lines inside buckling region in which the plate has the same maximum aerothermal deflections.

At flow angle $\Lambda = 45$ deg, the stability regions are shown in Fig. 12. Compared with the case of zero flow angle in Fig. 11, both the flat and the buckled regions are decreased due to a weaker stiffness in the 45-deg direction (e.g., λ_{cr} is 344 at $\Lambda = 45$ deg vs 532 at $\Lambda = 0$ deg), and the buckled region is upper bounded at $\lambda = 90$ vs 170 at $\Lambda = 0$ deg.

SMAHC Plates

With the embedding of SMA, the response of the SMAHC plates can be improved drastically. Figure 13 shows the stability regions for an SMAHC plate with (volume fraction $v_s = 10\%$ and prestrain of SMA $\varepsilon_r = 3\%$) at $\Lambda = 0$ deg. Compared with the traditional composite plate shown in Fig. 11, the flat and stable region of the SMAHC plate is enlarged greatly. The critical thermal buckling temperature ΔT_{cr} is increased greatly to 245°F (also shown in Fig. 4). It is interesting to note that the boundary λ_{cr} between the flat and stable region and the LCO flutter region first goes up as temperature increases, then goes down. This is due to the counteraction between thermal expansion effect of the composite matrix and the recovery force of SMA. Thermal expansion has the tendency to soften the plate and reduce λ_{cr}, whereas the SMA recovery force stiffens the plate and increases λ_{cr}. At low temperature, the SMA recovery force overcomes thermal expansion, the plate is stiffened, and λ_{cr} is

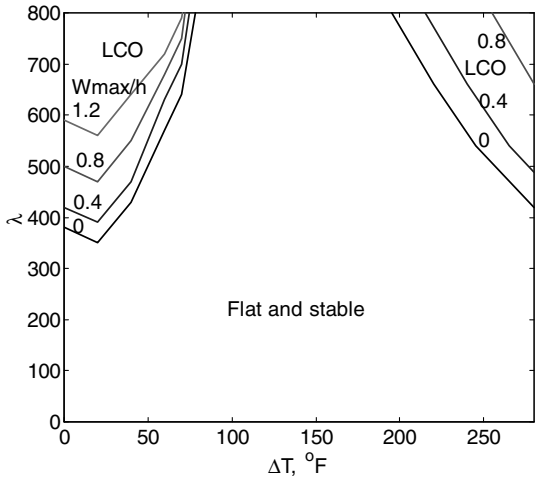

Fig. 16 W_{max}/h vs dynamic pressure and temperature of a clamped SMAHC ($v_s = 10\%$ and $\varepsilon_r = 5\%$) plate at $\Lambda = 45$ deg.

increased. With the increasing temperature, the SMA recovery force saturates, thermal expansion effect gradually becomes dominant, and the plate displays the reduced stiffness and reduced λ_{cr}. It is seen that at $\Delta T = 280$°F, the plate is buckled and the λ_{cr} is lower than that at T_{ref} or $\Delta T = 0$. Therefore, SMA volume fraction v_s and prestrain ε_r can be further adjusted to suppress the buckling completely and increase the λ_{cr} at high temperature. This is demonstrated by an increase of ε_r from 3 to 5% and keeping v_s at 10%.

For the SMAHC plate with $v_s = 10\%$ and $\varepsilon_r = 5\%$, as shown in Fig. 14, it is seen that the flat and stable region occupies most of the area. Compared with Fig. 13, the flat and stable region is further increased and the buckled region is completely suppressed and absent from the ΔT–λ domain investigated. Moreover, λ_{cr} at $\Delta T =$ 280°F is now much higher than even that at T_{ref}.

The effects of flow yaw angle $\Lambda = 45$ deg on the stability region are shown in Figs. 15 and 16 for the SMAHC plates with $v_s = 10\%$ and $\varepsilon_r = 3\%$ and $v_s = 10\%$ and $\varepsilon_r = 5\%$, respectively. Compared with the corresponding plots for flow angle $\Lambda = 0$ deg, the flat and stable region is slightly smaller.

Conclusions

A finite element procedure is presented for the determination of large-amplitude nonlinear panel flutter of SMAHC plates. Temperature-dependent material properties of SMA and traditional composites, as well as the von Kármán large deflection, are considered in the formulation. The concept of AEMs is introduced to further reduce the number of DOF for the first time in thermal flutter analysis by transferring nonlinear system equations in structural-node DOF to aeroelastic modal coordinates. The use of AEMs is validated and proved to be both accurate and efficient in numerical integration procedure. It is shown that flutter response of the plates embedded with SMA can be reduced and even suppressed for a large operational range of combination of dynamic pressure and temperature. Further investigations of SMAHC plates include high-temperature composite materials selection serving as a matrix for SMAHC, fatigue life estimation, and experiment verification.

References

[1] Dowell, E. H., Aeroelasticity of Plates and Shells, Noordhoff International, Leyden, The Netherlands, 1975.

[2] Mei, C., Abdel-Motagaly, K., and Chen, R., "Review of Nonlinear Panel Flutter at Supersonic and Hypersonic Speeds," *Applied Mechanics Reviews*, Vol. 52, No. 10, 1999, pp. 321–332.

[3] Dowell, E. H., "Nonlinear Oscillation of a Fluttering Plate 1," *AIAA Journal*, Vol. 4, No. 7, 1966, pp. 1267–1275.

[4] Dowell, E. H., "Nonlinear Oscillation of a Fluttering Plate 2," *AIAA Journal*, Vol. 5, No. 5, 1967, pp. 1856–1862.

[5] Ye, W. L., and Dowell, E. H., "Limit Cycle Oscillation of a Fluttering Cantilever Plate," *AIAA Journal*, Vol. 29, No. 11, 1991, pp. 1929–1936.

[6] Kuo, C. C., Morino, L., and Dugundji, J., "Perturbation and Harmonic Balance Methods for the Nonlinear Panel Flutter," *AIAA Journal*, Vol. 10, No. 10, 1972, pp. 1479–1484.
[7] Yuen, S., and Lau, S., "Effect of In-Plane Load on Nonlinear Panel Flutter by Incremental Harmonic Balance Method," *AIAA Journal*, Vol. 29, No. 9, 1991, pp. 1472–1479.
[8] Eastep, F., and McIntosh, S., Jr., "Analysis of Nonlinear Panel Flutter and Response under Random Excitation or Nonlinear Aerodynamic Loading," *AIAA Journal*, Vol. 9, No. 3, 1971, pp. 411–418.
[9] Morino, L., "A Perturbation Method for Treating Nonlinear Panel Flutter Problems," *AIAA Journal*, Vol. 7, No. 3, 1969, pp. 405–410.
[10] Olson, M. D., "Finite Element Approach to Panel Flutter," *AIAA Journal*, Vol. 5, No. 2, 1967, pp. 226–227.
[11] Olson, M. D., "Some Flutter Solutions Using Finite Element," *AIAA Journal*, Vol. 8, No. 4, 1970, pp. 747–752.
[12] Liaw, D. G., and Yang, T. Y., "Reliability and Nonlinear Supersonic Flutter of Uncertain Laminated Plates," *AIAA Journal*, Vol. 31, No. 12, 1993, pp. 2304–2311.
[13] Han, A. D., and Yang, T. Y., "Nonlinear Panel Flutter Using High Order Triangular Finite Element," *AIAA Journal*, Vol. 21, No. 5, 1983, pp. 1453–1461.
[14] Dixon, I. R., and Mei, C., "Finite Element Analysis of Large Amplitude Panel flutter of Thin Laminates," *AIAA Journal*, Vol. 31, No. 4, 1993, pp. 701–707.
[15] Gray, C. E., Jr., "Large Amplitude Finite Element Flutter Analysis of Composite Panels in Hypersonic Flow," Ph.D. Dissertation, Dept. of Aerospace Engineering, Old Dominion Univ., Norfolk, VA, 1991.
[16] Xue, D. Y., "A Finite Element Frequency Domain Solution of Nonlinear Panel Flutter with Temperature Effects and Fatigue Life Analysis," Ph.D. Dissertation, Dept. of Aerospace Engineering, Old Dominion Univ., Norfolk, VA, 1991.
[17] Abdel-Motagaly, K., Duan, B., and Mei, C., "Nonlinear Response of Composite Panels under Combined Acoustic Excitation and Aerodynamic Pressure," *AIAA Journal*, Vol. 38, No. 9, 2000, pp. 1534–1542; also *40th AIAA/ASME/ASCE/AHS/ASC Structures, Structural Dynamics & Materials Conference*, AIAA, Reston, VA, 1999, pp. 1963–1972.
[18] Abdel-Motagaly, K., Chen, R., and Mei, C., "Nonlinear Flutter of Composite Panels Under Yawed Supersonic Flow Using Finite Elements," *AIAA Journal*, Vol. 37, No. 9, 1999, pp. 1025–1032.
[19] Friedmann, P., and Hanin, M., "Supersonic Nonlinear Flutter of Orthotropic or Isotropic Panels with Arbitrary Flow Direction," *Israel Journal of Technology*, Vol. 6, Nos. 1–2, 1968, pp. 46–57.
[20] Chandiramani, N. K., Plaut, R. H., and Librescu, L., "Nonperiodic Flutter of a Buckled Composite Panel," *Sadhana*, Vol. 20, Parts 2–4, Apr.–Aug., 1995, pp. 671–689.
[21] Chandiramani, N. K., Plaut, R. H., and Librescu, L., "Nonlinear Flutter of Buckled Shear-Deformable Composite Panel in a High Supersonic Flow," *International Journal of Non-Linear Mechanics*, Vol. 30, No. 2, 1995, pp. 149–167.
[22] Zhou, R. C., Mei, C., and Huang, J. K., "Suppression of Nonlinear Panel Flutter at Supersonic Speeds and Elevated Temperatures," *AIAA Journal*, Vol. 34, No. 2, 1996, pp. 347–354.
[23] Abdel-Motagaly, K., "Finite Element Analysis and Active Control for Nonlinear Flutter of Composite Panels Under Yawed Supersonic Flow," Ph.D. Dissertation, Dept. of Aerospace Engineering, Old Dominion Univ., Norfolk, VA, 2001.
[24] Guo, X., and Mei, C., "Using Aeroelastic Modes for Nonlinear Panel Flutter at Arbitrary Supersonic Yawed Angle," *AIAA Journal*, Vol. 41, No. 2, 2003, pp. 272–279.
[25] Guo, X., and Mei, C., "Application of Aeroelastic Modes on Nonlinear Supersonic Panel Flutter at Elevated Temperatures," *Computers and Structures*, Vol. 84, Nos. 24–25, 2006, pp. 1619–1628.
[26] Houbolt, J. C., "A Study of Several Aerothermoelastic Problems of Aircraft in High Speed Flight," Ph.D. Dissertation, Inst. fur Flugzeugstatikund Leichtbau, Eidgenössische Technische Hochschule Zürich, Zürich, Switzerland, 1958.
[27] Xue, D. Y., and Mei, C., "Finite Element Nonlinear Panel Flutter with Arbitrary Temperatures in Supersonic Flow," *AIAA Journal*, Vol. 31, No. 1, 1993, pp. 154–162.
[28] Liaw, D. G., "Nonlinear Supersonic Flutter of Laminated Composite Plates Under Thermal Load," *Computers and Structures*, Vol. 65, No. 5, 1997, pp. 733–740.
[29] Zhou, R. C., "Finite Element Analysis for Nonlinear Flutter Suppression of Composite Panels at Elevated Temperatures Using Piezoelectric Materials," Ph.D. Dissertation, Dept. of Aerospace Engineering, Old Dominion Univ., Norfolk, VA, 1994.
[30] Rogers, C. A., Liang, C., and Jia, J., "Behavior of Shape Memory Alloy Reinforced Composite Plates, Part 1: Model Formulation and Control Concepts," *30th AIAA/ASME/SAE/ASEE Joint Propulsion Conference & Exhibit* , AIAA, Washington, D.C., 1989, pp. 2011–2017.
[31] Rogers, C. A., Liang, C., and Barker, D. K., "Dynamic Control Concept Using Shape Memory Alloy Reinforced Plates," *Smart Materials, Structures and Mathematical Issues*, Technomic, Lancaster, PA, 1989, pp. 39–62.
[32] Duan, B., Tawfik, M., Ro, J. J., and Mei, C., "Vibration of Laminated Composite Plates Embedded with SMA at Elevated Temperatures," 7th Annual International Symposium on Smart Structures and Materials, Newport Beach, CA, International Society for Optical Engineering (SPIE) Paper 3991-46, Mar. 2000.
[33] Lee, J. J., and Choi, S., "Thermal Buckling and Postbuckling Analysis of a Laminated Composite Beam with Embedded SMA Actuators," *Composite Structures*, Vol. 47, Nos. 1–4, 1999, pp. 695–703.
[34] Lee, H. J., Lee, J. J., and Huh, J. S., "A Simulation Study on the Thermal Buckling Behavior of Laminated Composite Shells with Embedded Shape Memory Alloy (SMA) Wires," *Composite Structures*, Vol. 47, Nos. 1–4, 1999, pp. 463–469.
[35] Suzuki, S., and Degaki, T., "Supersonic Panel Flutter Suppression Using Shape Memory Alloy," *International Journal of Intelligent Mechatronics: Design and Production*, Vol. 3, No. 1, 1998, pp. 1–10.
[36] Tawfik, M., Duan, B., Ro, J. J., and Mei, C., "Suppression of Postbuckling Deflection and Panel Flutter Using Shape Memory Alloy," 7th Annual International Symposium on Smart Structures and Materials, Newport Beach, CA, International Society for Optical Engineering (SPIE) Paper 3991-44, Mar. 2000.
[37] Nowacki, W., *Thermoelasticity*, Addison Wesley Longman, Reading, MA, 1962.
[38] Bogner, F. K., Fox, R. L., and Schmit, L. A., "The Generation of Inter-Element Compatible Stiffness and Mass Matrices by the Use of Interpolation Formulas," U.S. Air Force Flight Dynamics Laboratory Rept. TR-66-80, Wright-Patterson AFB, OH, 1966, pp. 396–443.
[39] Cross, W. B., Kariotis, A. H., and Stimler, F. J., "Nitinol Characterization Study," NASA CR-1433, 1970; also Goodyear Aerospace Corp. Rept. Ger 14188, Akron, OH.